CHAPTER 6: Cd doped $Ag_2O/BiVO_4$ photocatalysts

6.1 Introduction

Doping a semiconductor photocatalyst can change its electronic structure and induce charge separation, resulting in delayed recombination (Gong et al., 2020; Haiping Li et al., 2020; Jianbin Liu et al., 2021; Murali et al., 2021; Negishi et al., 2012). The bandgap, valence band (VB), or conduction band (CB) positions are also affected. For instance, Natu et al. reported cobalt doping shifts the VB position of NiO (Natu et al., 2012). In another study, Wang et al. executed a detailed DFT investigation of the effect of oxygen doping on the Ta_3N_5 photocatalyst. The oxygen doping changed the bandgap and band edges of the Ta_3N_5 photocatalyst (Jiajia Wang et al., 2014). Doping also affects the adsorption properties of the parent photocatalyst (Andjelkovic et al., 2014; Jie Chen et al., 2020; Panneri et al., 2017). Hence, doping affects the photocatalyst's bandgap, band positions, and adsorption behavior. Therefore, doping could effectively produce a new photocatalyst with different photocatalytic properties.

More intensive use of medium and small bandgap (corresponding to the visible range) semiconductors is necessary for fabricating photocatalysts that can optimally utilize the UV-visible part of the solar spectrum. For instance, photostability or photo corrosion of (small bandgap) Ag_2O has hampered its photocatalytic applications. Doping Ag_2O or its composite formation with another photocatalyst could significantly reduce the problem while improving excited species charge separation (H. Xu et al., 2018). A recent DFT study on Zn-doping in Ag_2O revealed that such inclusion could shift the VB of the Ag_2O to a higher positive value (De et al., 2020). In another report, Sr doping also resulted in Ag_2O bandgap widening (Kiani et al., 2019). Recently, De et

al. showed that Ni doping could shift the VB and CB edge of the Ag_2O photocatalyst to a more positive and less negative value. The higher valence Ni^{2+} substituted Ag^{+} to give the host system excess electrons (De & Sinha, 2022). Thus, the strategy of doping Ag_2O can provide a photocatalyst with a tunable band structure with distinct properties.

Doping and composite formation with another semiconductor can change a photocatalyst's reduction and oxidation driving forces along with the excited species charge separation. Hence, a doped Ag_2O material as part of a composite should give an improved photocatalyst. There have been a few investigations on Ag_2O-based composites (or photocatalytic heterostructures). For instance, there are reports on the fabrication and evaluation of $ZnO/Ag/Ag_2O$, Ag_2O/TiO_2, $BiVO_4/Ag/Ag_2O$, Ag_2O/Bi_2O_3, etc., photocatalysts (L. Chen et al., 2019; Sahu & Das, 2022; Ullah et al., 2020; L. Zhu et al., 2012). But to date, we have not encountered any doped Ag_2O-based heterojunction or composite photocatalyst.

In the present research, we investigated the photocatalytic properties of Cd-doped Ag_2O, and its composite with $BiVO_4$. Note that neither synthesis nor the photocatalytic properties of Cd doped-Ag_2O have been reported in published literature. The first part of this research evaluated whether Cd substitutes Ag or occupies an interstitial position through density functional theory (DFT) calculation of the formation energies of the two models. Simultaneously, Cd-doped Ag_2O nanoparticles were prepared by a hydrothermal precipitation protocol. X-ray diffraction (XRD) results agreed with the DFT defect formation energy prediction. X-ray photoelectron spectroscopy (XPS) investigated the chemical species and the VB position in the Cd-doped Ag_2O nanoparticles. Separately, a well-established hydrothermal protocol was employed to prepare monoclinic $BiVO_4$. In the next step, another hydrothermal strategy joined these nanoparticles to Cd-doped Ag_2O nanostructures. The prepared composite

particles were characterized using different techniques. The composite nanoparticles were evaluated for photocatalytic ciprofloxacin (CIP) degradation activity under visible light irradiation. CIP is frequently administered to human patients and excreted in a partially metabolized state. The latter makes the target microorganisms in the environment resistant to the antibiotic in question. Photocatalytic activities with different active species scavenger molecules probed the underlying photocatalysis mechanism. Parallelly, DFT calculations ascertained the adsorption energies of oxygen and H_2O on the Cd-doped Ag_2O and $BiVO_4$ surfaces. The information collated was used to propose a plausible photocatalysis mechanism.

6.2 Experimental

6.2.1 Sample preparation

6.2.1.1 Synthesis of Cd doped Ag_2O

A hydrothermal protocol was followed to prepare Cd-doped Ag_2O. Two millimoles (mmol) of $AgNO_3$ (Merck) were fully dissolved in 50 ml deionized double distilled water (DDDW) with continuous stirring on a magnetic stirrer. Then, 0.2M NaOH was added drop-by-drop into the stirring solution until the solution pH reached 11. A brown-colored precipitate was formed during the addition. The stirring was continued for 15 minutes. Next, the desired amount of $Cd(NO_3)_2.4H_2O$ (Merck) aqueous solution was added to the previously obtained mixture. Stirring was continued for another 15 minutes, and then the reaction mixture was transferred to a 100 ml stainless steel autoclave. The latter was put in a hot air oven at 180°C for 24 hours. We prepared three different compositions of Cd-doped Ag_2O samples abbreviated as D1, D2, and D3. These contained 0.3, 0.62, and 1.25-mole percent of $Cd(NO_3)_2.4H_2O$. In addition, the

pure Ag_2O (denoted as D0) was also synthesized by the same hydrothermal protocol but without $Cd(NO_3)_2.4H_2O$ addition.

6.2.1.2 Synthesis of $BiVO_4$

Aqueous solutions of $Bi(NO_3)_3.5H_2O$ (Merck) and NH_4VO_3 (HIMEDIA) were prepared in two separate beakers. In one beaker (A), 20 ml of 4M HNO_3 was directly mixed with 4 mmol of $Bi(NO_3)_3.5H_2O$ salt with continuous stirring until the formation of a clear solution. In another beaker (B), 4 mmol of NH_4VO_3 was dissolved in 20 ml of 4M NaOH by continuous stirring. Stirring was continued in both beakers for 30 minutes. The solution in beaker B was added drop-by-drop into beaker A in the next step. The formation of a yellow-colored precipitate was observed. Next, the reaction mixture pH was adjusted to 7 by adding an appropriate amount of NaOH. This reaction mixture was stirred for another 25 minutes and then transferred to a 100 ml autoclave reactor for hydrothermal treatment at 180°C. After 20 hours of hydrothermal treatment, the reaction mixture was allowed to cool. The precipitate formed was separated and washed with DDDW several times until the water used in washing had neutral pH. Finally, the as-prepared precipitate was rewashed with ethanol and dried at 60°C under a hot air oven to get the $BiVO_4$ nanoparticles (abbreviated by 'V0' in the rest of the Chapter).

6.2.1.3 Synthesis of $BiVO_4$/Cd-doped Ag_2O

The D1 sample (of Cd-doped Ag_2O) was mixed with 5, 10, and 20 weight% of $BiVO_4$ nanoparticles in 60 ml DDDW to prepare three separate systems abbreviated as D1/5V, D1/10V, and D1/20V. The three mixtures were stirred for 4 hours to induce interaction between Cd-doped Ag_2O and $BiVO_4$ nanoparticles. These mixtures were transferred to 100 ml autoclave reactors and subjected to hydrothermal treatment for

twelve hours at 120°C. Afterward, the prepared material was separated from the supernatant and dried at 50°C overnight in a hot air oven.

6.2.2 Computational methods

The plane-wave density functional theory (DFT) calculations were done on the Medea VASP (Vienna ab-initio simulation package) software. The calculations used generalized gradient approximation Perdew-Burke-Ernzerhoff (GGA-PBE) exchange-correlation functional and the projected augmented wave (PAW) pseudopotentials. A $2 \times 2 \times 2$ supercell was built from the Ag_2O unit cell (ICDS Card No. 4318188) and was optimized using $2 \times 2 \times 2$ k-points and 520 eV energy cut-off. The optimized supercell is labeled as P0 in the rest of the chapter. The doped Cd atom could substitute an Ag atom or occupy an interstitial position in the Ag_2O lattice. Thus, in one model (denoted as P1), one Cd substituted an Ag atom in the Ag_2O supercell. In another model (denoted as P2), a Cd atom was placed in an interstitial position of the Ag_2O lattice. These two models were optimized with the same calculation parameters as mentioned above. After that, the defect formation energies of the two doped systems were calculated using the following equations.

$$E_f(Sub) = E_{defect}(P1) - [E_{perfect}(P0) - \mu_{Ag} + \mu_{Cd}] \quad (6.1)$$

$$E_f(Inter) = E_{defect}(P2) - [E_{perfect}(P0) + \mu_{Cd}] \quad (6.2)$$

Here, $E_f(Sub)$ and $E_f(Inter)$ are the defect formation energy of the substituted and interstitially doped systems. $E_{defect}(P1)$, $E_{defect}(P2)$, and $E_{perfect}(P0)$ are the energies of the P1, P2, and P0 models, respectively. The energy per atom in Ag and Cd metallic unit cells gives the chemical potentials of the Ag and Cd (μ_{Ag} and μ_{Cd}). The adsorption energies (E_{abs}) of H_2O and O_2 on Cd-doped Ag_2O (200) and $BiVO_4$ (112) surfaces were evaluated by slab model calculations using equation 6.3. First, the Ag_2O

supercell was cleaved to obtain its (200) surface, and then an Ag atom was replaced with a Cd atom to construct the Cd-doped Ag_2O (200) slab. Similarly, the $BiVO_4$ supercell was cleaved to get its (112) surface. A four-layer slab with a vacuum of 10 Å was considered for both models. The slab dimensions for Cd doped Ag_2O (200) and $BiVO_4$ (112) surfaces were $6.69 \times 6.69 \times 28.92$ and $6.93 \times 7.32 \times 96.99$, respectively.

$$E_{abs} = E_{slab+adsorbate} - (E_{slab} + E_{adsorbate}) \quad (6.3)$$

Here, $E_{slab+adsorbate}$ is the energy of the slab with the adsorbate molecule. E_{slab} and $E_{adsorbate}$ are the energies of the individual free slab and the free adsorbate molecule.

6.2.3 Photocatalytic experiment details

A 2 ml aqueous solution of CIP (10 ppm) at pH~3 and 100μl of the re-dispersed photocatalyst aqueous suspension (1 mg/ml) were mixed properly in a 4 ml quartz cuvette. The mixture was allowed to stand in a dark environment for 35 minutes under continuous stirring until adsorption-desorption equilibrium. Then the cuvette was kept under visible light irradiation (14W Philips LED bulb with an intensity of 720 W/m^2). The absorbance of the reaction mixture was recorded at regular time intervals to monitor the photocatalytic activities of the synthesized materials. Turnover frequencies (TOF) were also calculated.

6.3 Results and discussion

6.3.1 Structural properties

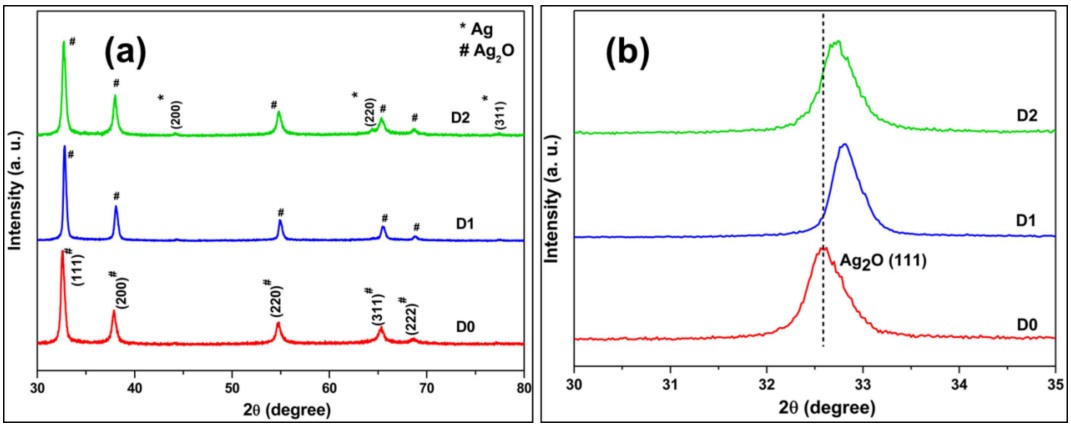

Figure 6.1 (a) The powder XRD patterns of undoped (D0) and doped samples (D1 and D2) (b) the zoomed-in Ag_2O (111) peak part.

Figure 6.1(a) displays the powder XRD pattern of the undoped (D0) and different Cd-doped Ag_2O nanoparticle samples (D1 and D2). All the peaks in the XRD plots of D0 and D1 match the standard FCC Ag_2O (JCPDS Card No. 75-1532) pattern. Other phases are not present in the D1 sample. Nonetheless, the XRD of D2, in addition to the FCC Ag_2O peaks, also clearly displays three small peaks of the FCC Ag phase. The formation of reduced Ag is due to the excess electrons supplied by the dopant when added beyond a specific limit. Furthermore, the XRD pattern of sample D3 displayed peaks of phases other than FCC Ag_2O and Ag (Figure 6.2) when the dopant level increased to 1.25 mol%. CdO_2 peaks in Figure 6.2 are matched with the standard JCPDS database Card No.391221, which is cubic primitive (space group: $Pa\bar{3}$) crystal structure of CdO_2.

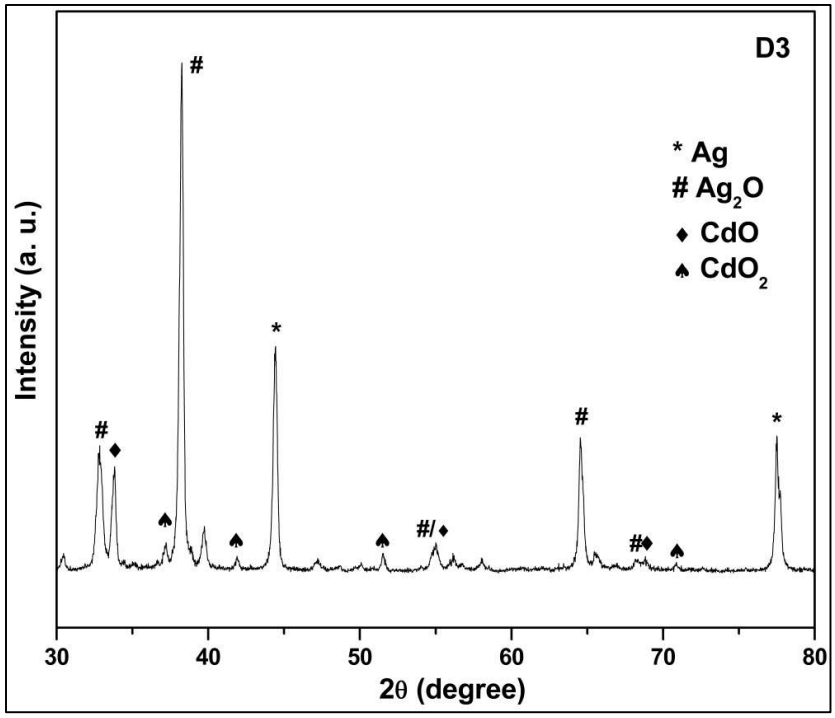

Figure 6.2 Powder XRD pattern of D3 sample.

Figure 6.1(b) compares the (111) plane peak positions of D0, D1, and D2 samples. The (111) peak position shifts towards higher 2θ regions in doped samples, indicating lattice contraction. Nevertheless, the peak shift is not uniform. The smallest dopant percentage sample (D1) gave the maximum peak shift. The Cd^{2+} and Ag^{+} have effective ionic radii of 95 and 115 pm. As mentioned earlier, the dopant (Cd^{2+}) has two choices: it can substitute one Ag or go into the interstitial sites in the Ag_2O lattice. Lattice contraction is only viable if smaller Cd substitutes Ag in the Ag_2O lattice. The D1 dopant sample was selected to prepare composite materials with $BiVO_4$ since it showed substitutional doping of Cd in the Ag_2O lattice without FCC Ag formation.

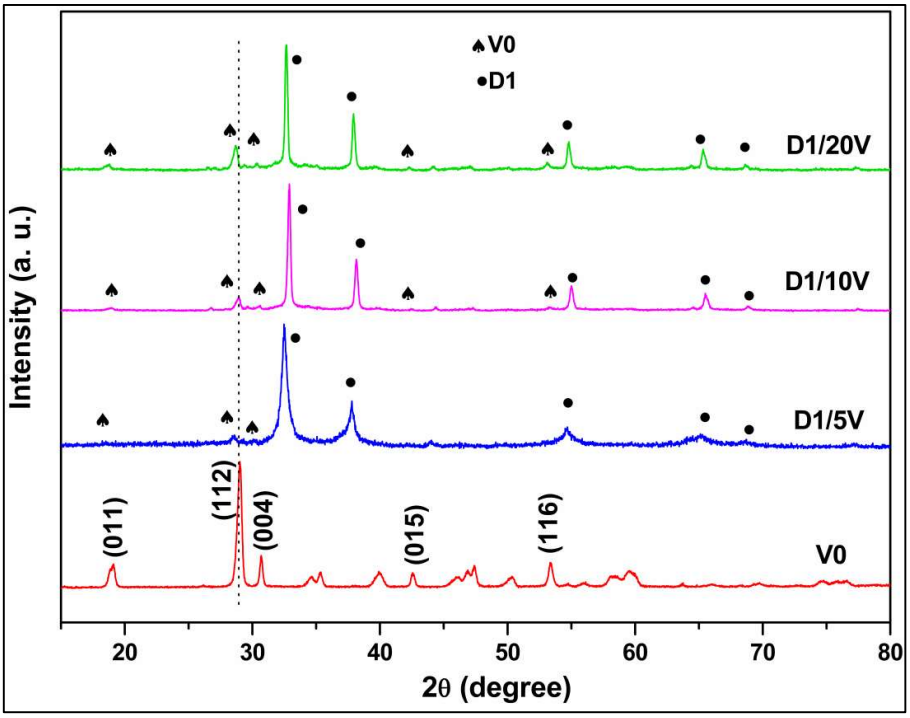

Figure 6.3 Comparison of powder XRD pattern of $BiVO_4$ nanoparticles and composite samples (D1/5V, D1/10V, D1/20V).

Figure 6.3 compares the powder XRD patterns of the composite materials with those of $BiVO_4$ (V0) and D1 samples. The XRD pattern of sample V0 matches the standard body-centered monoclinic (JCPDS Card No. 831699) phase of $BiVO_4$. The major peaks in the XRD at 18.9°, 29°, 30.7°, 42.5°, and 53.4° are indexed to the (011), (112), (004), (015), and (116) planes of the body-centered monoclinic $BiVO_4$. The XRD of all composite samples showed the presence of both Ag_2O and $BiVO_4$ phases, indicating nanocomposite formation (Jatav et al., 2021). Hereafter, the investigation concentrates on D1/10V sample characterization because of its enhanced photocatalytic activity (compared to D1/5V and D1/20V composites) towards CIP. Figure 6.4(a) and (b) exhibit the TEM and high-resolution TEM (HRTEM) images of the D1/10V composites. The high-resolution image of the encircled region (in Figure 6.4a) shows

two types of fringes adjacent to each other. These fringe spacings match the d-spacing of $BiVO_4$ (011) and Ag_2O (111) planes, confirming D1/10V composite formation.

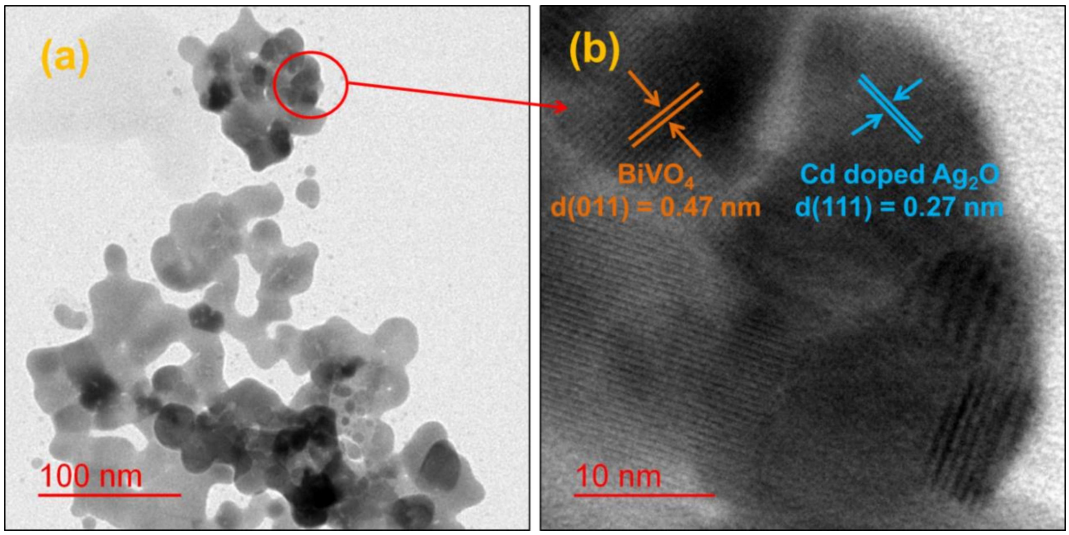

Figure 6.4 (a) TEM and (b) HRTEM images of the D1/10V sample.

6.3.2 XPS analysis

XPS investigation gives information about elements and their oxidation states in a material. Figure 6.5 shows the Ag 3d high-resolution XPS plots of samples D0 and D1. The Ag $3d_{3/2}$ and Ag $3d_{5/2}$ peaks at 374.28 and 368.26 eV for D0 shift to 373.75 and 367.73 eV for the D1 sample. The extra electrons injected into the system by the Cd dopant made D1 electron-rich, causing the shift of respective Ag 3d peaks to lower binding energies.

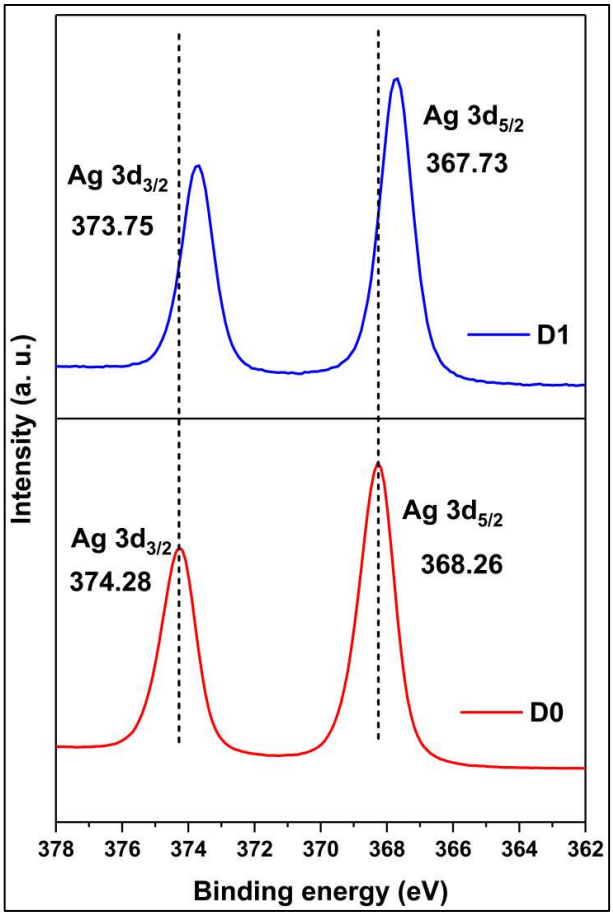

Figure 6.5 Comparison of high-resolution Ag3d spectra of D0 and D1 samples.

The XPS survey spectrum of the D1/10V composite shows the presence of Ag, Bi, V, and O elements in the composite (see Figure 6.6).

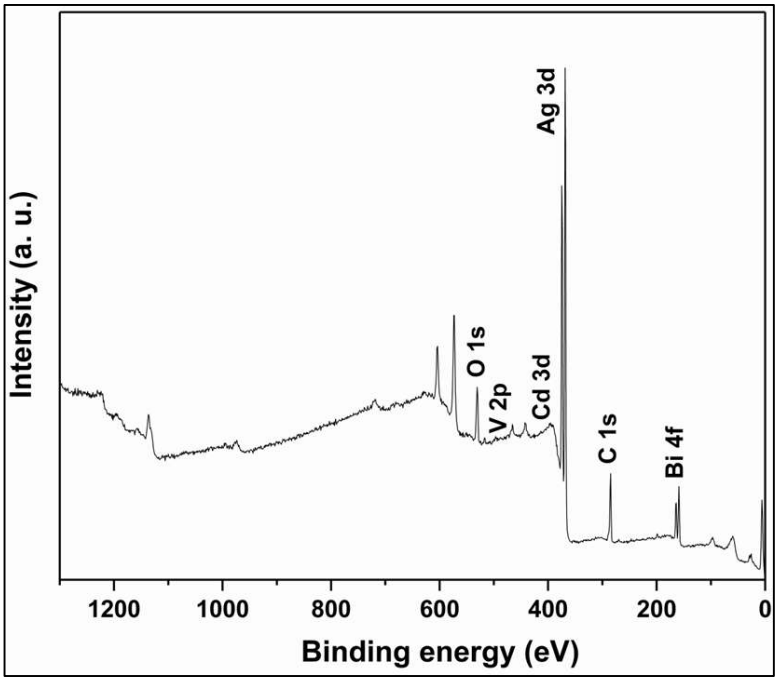

Figure 6.6 XPS survey spectrum of D1/10V sample.

Figure 6.7(a) compares the Ag 3d region high-resolution XPS plots of D1 and D1/10V samples. The Ag $3d_{5/2}$ and Ag $3d_{3/2}$ peaks at 367.71 and 373.74 eV for D1 shifted to higher values (Ag $3d_{5/2}$ at 368.15 and Ag $3d_{3/2}$ at 374.18 eV) in the D1/10V composite spectrum. Simultaneously, the Bi 4f spectrum with two peaks corresponding to Bi $4f_{7/2}$ at 158.96 and Bi $4f_{5/2}$ at 164.26 eV shifted to lower binding energy in the composite sample (Bi $4f_{7/2}$ at 158.70 and Bi $4f_{5/2}$ at 164.01 eV) (see Figure 6.7b). The shift to higher binding energies of Ag 3d peaks and lower binding energies of the Bi 4f peaks implies electron transfer from the Cd doped Ag_2O (D1) to $BiVO_4$ (V0). Figure 6.7(c) and (d) display the valence band XPS plots of D1 and D1/10V samples. The VB edge of the D1 sample is at 2.67eV, and $BiVO_4$ (V0) is at 1.34 eV. Note that the VB position of the D0 (undoped Ag_2O) sample is at 0.8 eV. Hence, Cd-doping of Ag_2O causes a severe shift in the VB position of the sample. A Z-scheme electron transfer mechanism seems to operate in this composite since the component with more negative

CB ($BiVO_4$) becomes electron-rich, while the Cd-doped Ag_2O part becomes electron-deficient.

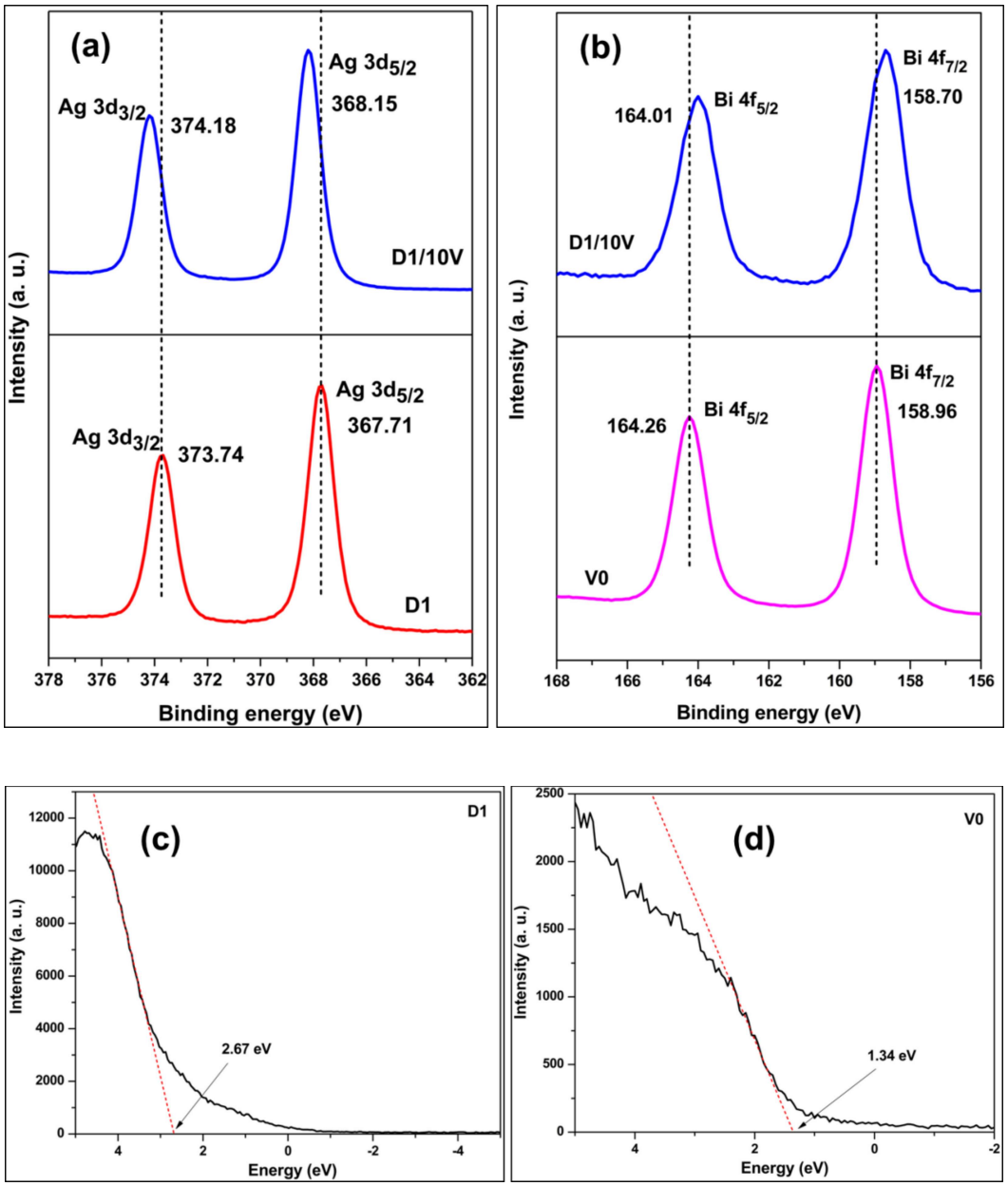

Figure 6.7 (a) Ag 3d comparison of D1 and D1/10V (b) Bi 4f comparison of V0 and D1/10V, the valence band XPS of (c) D1, and (d) V0.

6.3.3 The bandgap

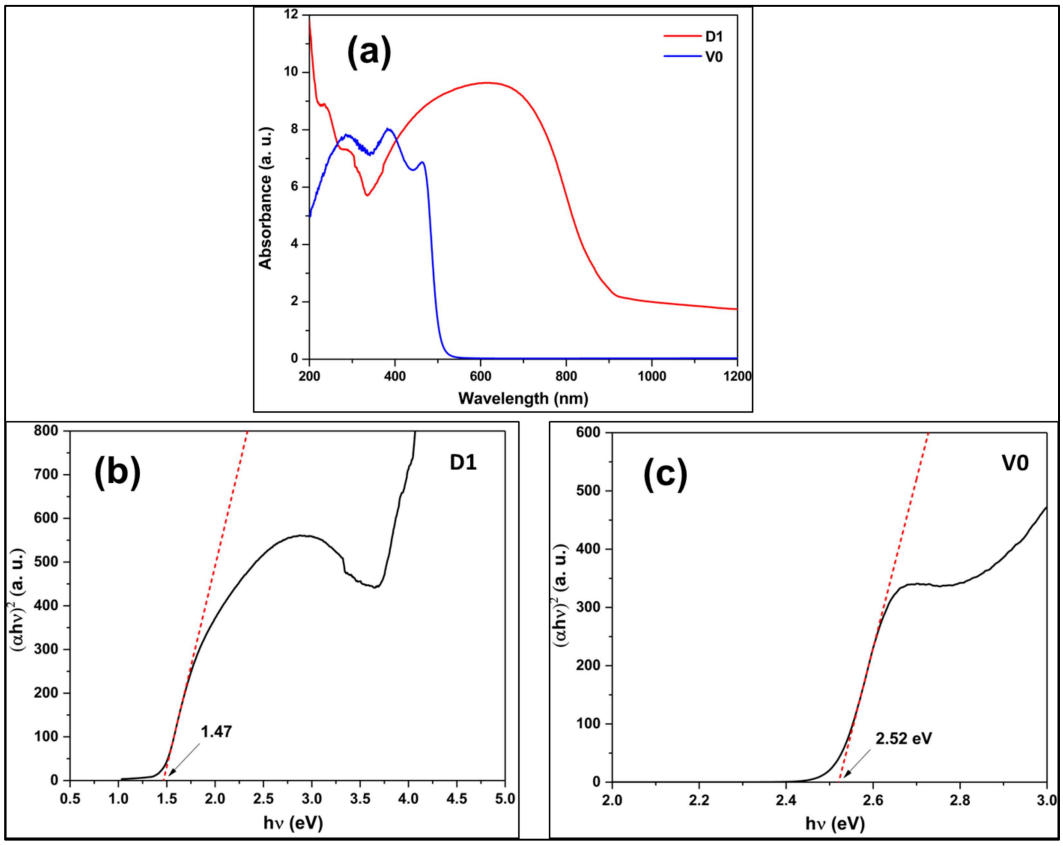

Figure 6.8 (a) UV-visible absorption spectrum of D1 and V0 samples. The Tauc plot of (b) D1 and (c) V0.

The bandgap of a photocatalyst is essential for proposing a reasonable photocatalytic mechanism. The Tauc plot is derived from the solid-state UV-visible absorption data using equation (6.4).

$$(\alpha h\nu)^{1/n} = (h\nu - E_g) \qquad (6.4)$$

The x-axis intercept of the fit to the linear part of the Tauc plot gives the bandgap (E_g) of the tested material. Figure 6.8(a) represents UV-Visible absorption data of the D1 and V0 samples in solid powder form. The Tauc plots of D1 and V0 samples show direct bandgaps of 1.47 and 2.52 eV, respectively (see Figure 6.8(b) and (c)).

Combining the VB positions and the bandgaps of D1 and V0 samples gives us their relative CB positions. Thus, the CB of D1 is at 1.19 eV and V0 at -1.18 eV.

6.3.4 Electrochemical studies

Electrochemical impedance spectroscopy (EIS) measurements are associated with the charge carrier's recombination kinetics. Figure 6.9a displays the Nyquist plots for the D1, V0, and D1/10V photocatalyst samples. These plots help to interpret the charge transfer resistance based on the size of the semicircle formed. The smaller radius of the circle indicates lower charge transfer resistance (or better charge transfer kinetics) and consequences decrease in electron-hole pair recombination (Ajith & John, 2022; Bootluck et al., 2021, 2022; Duan et al., 2022; Güy, 2020; S. Huang et al., 2021; Nawaz et al., 2022; Thenmozhi et al., 2022). Hence, photocatalytic reaction becomes faster. The D1/10V composites showed lower semicircle diameter, indicating a better charge separation than its components. The Mott-Schottky plot of the D1 catalyst is given in Figure 6.9b. The positive slope of the plot gave proof of n-type conductivity in the D1 material.

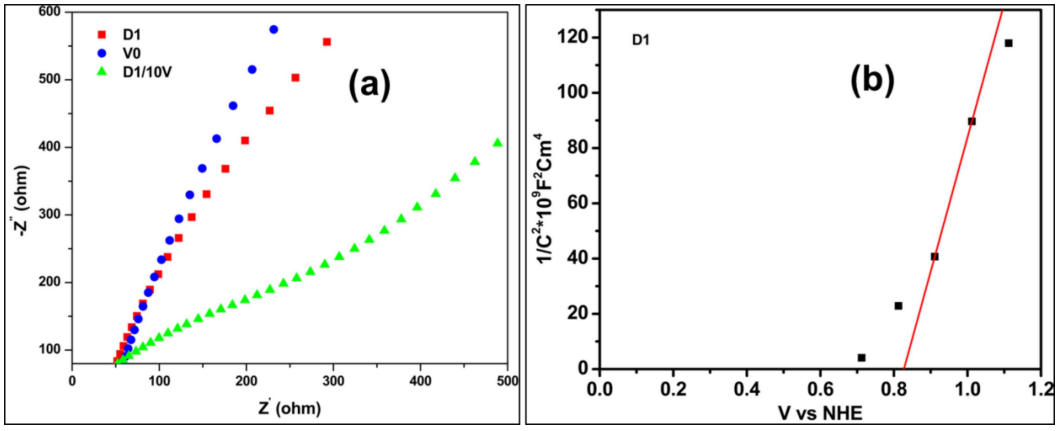

Figure 6.9 (a) Nyquist plots for D1, V0, and D1/10V (b) Mott-Schottky plot of D1.

6.3.5 DFT results

The DFT calculation supports the experimental results and helps to develop a plausible mechanism during the photocatalytic reaction. The formation energy was calculated using equations (1) and (2) in section 6.2.2. The formation energies of P1 (substitutional) and P2 (interstitial) models are -0.43 and 0.53 eV, respectively. Thus, substitutional doping is more favorable than interstitial doping, in agreement with the XRD result.

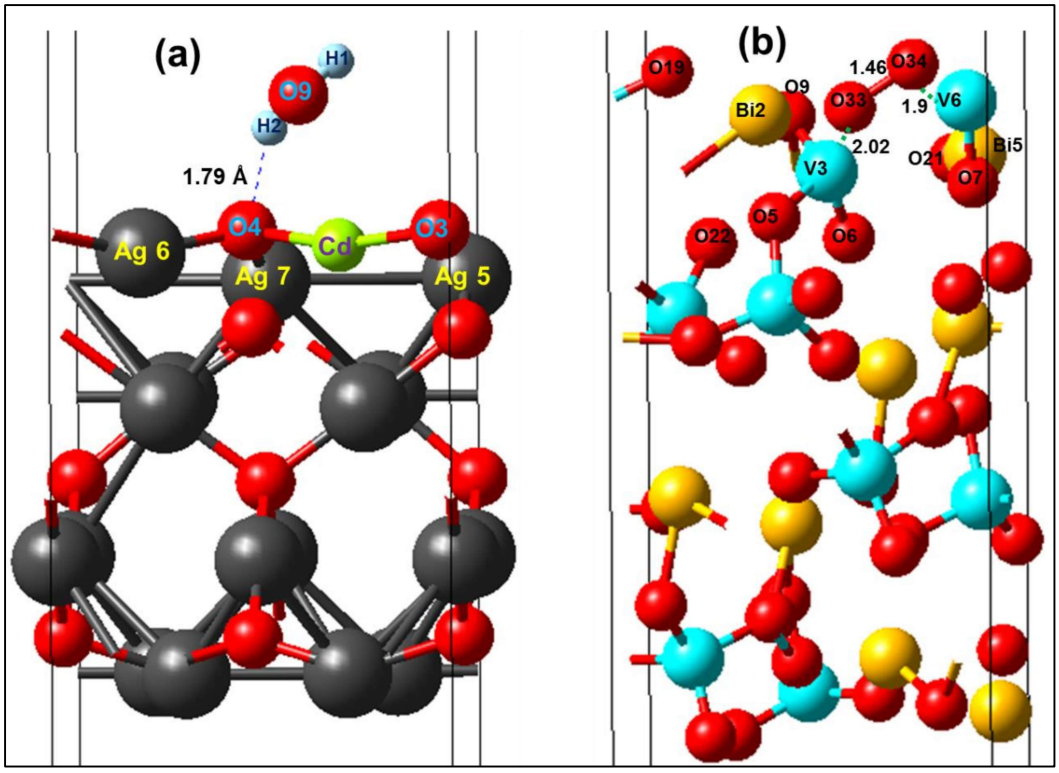

Figure 6.10 DFT calculation of (a) H_2O interaction with the Cd-doped Ag_2O (200) surface and (b) O_2 interaction with $BiVO_4$ surface.

Table 6.1 tabulates the adsorption energies of H_2O and O_2 adsorption on Cd-doped Ag_2O and $BiVO_4$ surfaces. It also gives distances between different atoms in the adsorbate molecule and those on the adsorbent surface. The adsorption energies show that H_2O adsorption on the Cd-doped Ag_2O surface is more favorable than $BiVO_4$.

Similarly, O_2 adsorption on the $BiVO_4$ surface gave more negative energy than on the Cd-doped Ag_2O surface. Figure 6.10(a) and (b) show adsorption of H_2O on Cd-doped Ag_2O (200) surface and O_2 molecule on $BiVO_4$ (112) surface. The H_2O molecule adsorbed on the Cd-doped Ag_2O surface via a hydrogen bond (distance = 1.79 Å) between H(2) (in H_2O) and O(4) (in Cd-doped Ag_2O surface). Upon the interaction with the Cd-doped Ag_2O surface, one of the O-H bonds in the H_2O molecule got elongated from 0.97 to 1.00 Å (in Table 6.1), indicating H_2O activation on the Cd-doped Ag_2O surface. Similarly, the O_2 molecule interacted with vanadium (shown by the dotted line in Figure 6.10b) on the $BiVO_4$ surface. The O_2 bond elongated from 1.24 to 1.46 Å (in Table 6.1), showing O_2 activation on the $BiVO_4$ surface.

Table 6.1 Adsorption energies and interatomic distances for adsorption of H_2O and O_2 on considered Cd-doped Ag_2O and $BiVO_4$ surfaces.

Slab surface	**E_{ads} (eV)**		**Distance (Å)**		
	H_2O	**O_2**		**Before adsorption**	**After adsorption**
Cd doped Ag_2O (200)	-1.56	-1.68			
			H1-O9	0.97	0.97
			H2-O9	0.97	1.00
			H2-O4	1.75	1.79
	-0.27	-4.39	**O33-O34**	1.24	1.46
$BiVO_4$ (112)			**V3-O33**	1.82	2.02
			V6-O34	1.81	1.90

6.3.6 Photocatalytic properties

The photocatalytic activity of the synthesized materials was evaluated for visible light photodegradation of CIP. Figure 6.11a compares the photocatalytic activities of

different samples towards CIP photodegradation. The D1/10V composite exhibits the maximum photocatalytic activity. It is also reflected in the synthesized photocatalysts' (D1, V0, D1/5V, D1/10V, and D1/20V) turnover frequency (TOF) and rate constant values (see Table 6.2). Figure 6.11b shows that the CIP degradation results on D1, V0, and their composites follow pseudo-first-order reaction kinetics. The following equation expresses the first-order reaction kinetics,

$$-\ln(C/C_0) = k_{app}t \qquad (6.5)$$

Here, C_0 is the initial CIP concentration in the aqueous medium, C denotes the CIP concentration at time t, k_{app} is the apparent rate constant, and t is photocatalysis reaction time. Photocatalysis experiments were performed with scavengers like isopropyl alcohol (IPA) for hydroxyl radicals, KI for holes, and p-benzoquinone (PBQ) molecules for superoxide radicals. Figure 6.11c displays the results of the scavenging experiments on the photocatalyst D1/10V. The presence of IPA gives higher catalytic activity compared to without scavenger. The IPA can also act as an electron donor and increase charge separation during photocatalysis.

On the contrary, the photocatalytic activity is drastically reduced in the presence of KI and PBQ scavengers. It indicates that both holes and superoxides contribute to photocatalytic CIP degradation. Figure 6.11d shows reusability results during the photocatalysis of the D1/10V sample. This photocatalyst shows high recyclability compared to the D1 catalyst. Thus, D1 alone is not a good photocatalyst for CIP degradation. But it is an efficient photocatalyst for CIP degradation as a composite with $BiVO_4$.

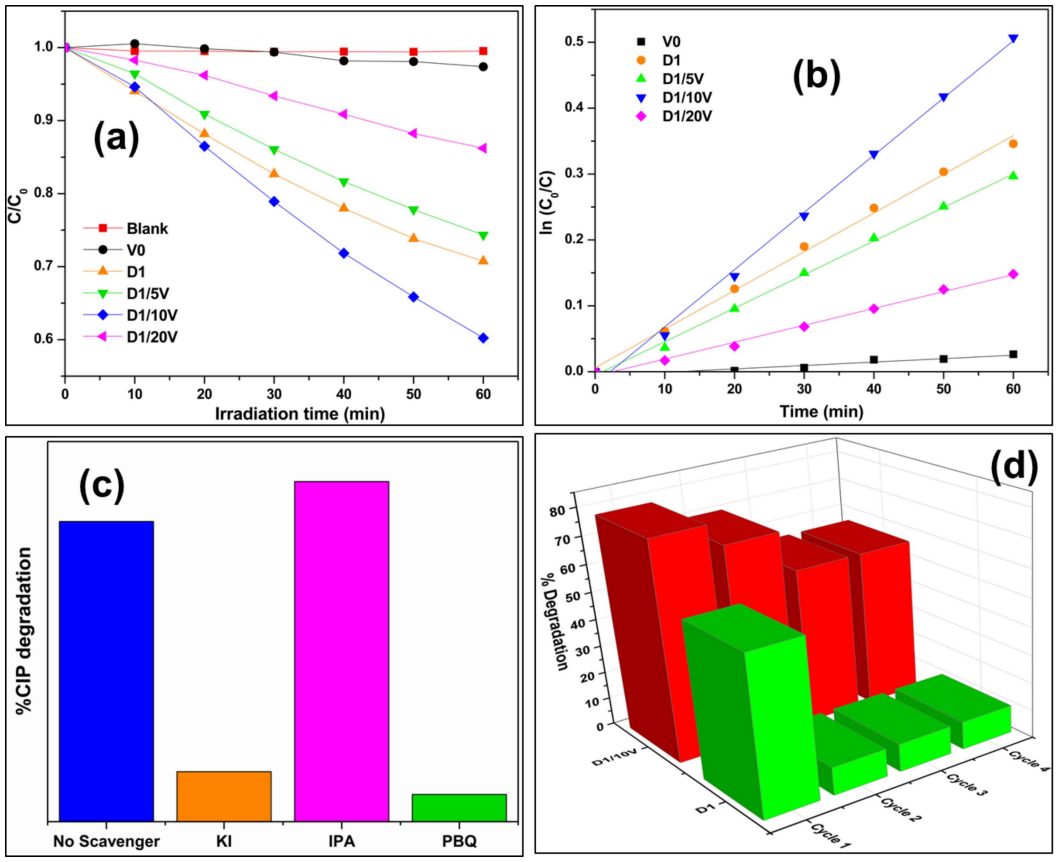

Figure 6.11 (a) Comparison of CIP photodegradation for composites samples with component catalyst (b) kinetics plot comparison (c) scavenger experiment on D1/10V catalyst (d) catalytic recyclability for D1 and D1/10V catalysts.

Table 6.2 Turnover frequency (TOF) and rate constant of synthesized catalysts for the photo-degradation of CIP.

Catalysts	TOF (mole $g^{-1}min^{-1}$)	Rate constant (k_{app}) (min^{-1})
D1	2.25×10^{-6}	5.9×10^{-3}
V0	3.17×10^{-7}	0.5×10^{-3}
D1/5V	2.06×10^{-6}	5.1×10^{-3}
D1/10V	2.97×10^{-6}	8.7×10^{-3}
D1/20V	7.58×10^{-7}	2.6×10^{-3}

Two additional control photocatalytic experiments were performed by replacing water with acetonitrile (MeCN) as the solvent. The first experiment was done without oxygen purging. No CIP degradation (as shown in Figure 6.12a) was observed under these circumstances. The second control experiment checked CIP degradation in MeCN medium and O_2 purging. In contrast to the first experiment, this time, there was a little CIP degradation (see Figure 6.12b). It indirectly proved CIP is oxidized by VB photoexcited holes with the help of externally purged O_2. The first control experiment shows that CIP degradation does not occur without water. Earlier scavenger experiments have already shown that superoxides are the dominant active species in CIP degradation. Superoxide radicals can be generated only by reducing oxygen molecules. The latter's sustained source can only be water oxidation (in the absence of any other substance in the reaction mixture). Thus, these two MeCN control experiments show that water oxidation plays a role in CIP degradation, and CIP cannot be photocatalytically degraded without water (Kofuji et al., 2018).

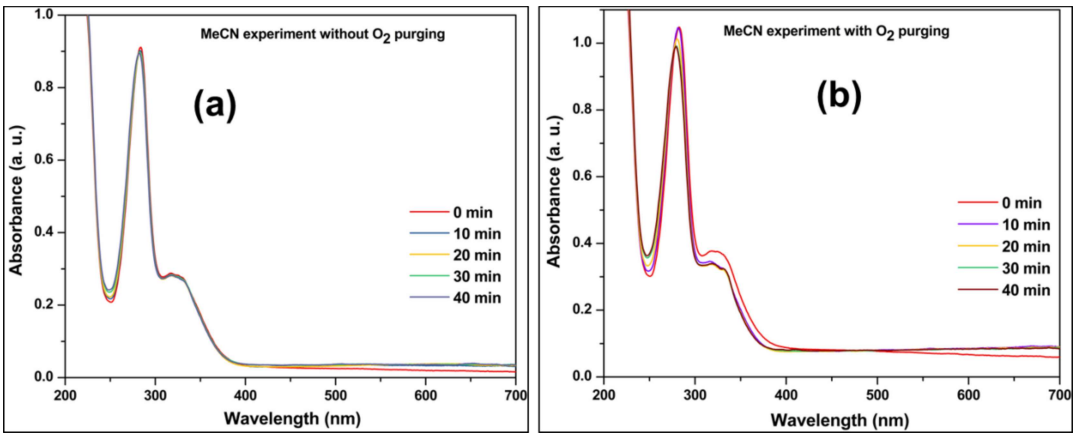

Figure 6.12 UV-Vis absorbance spectra of CIP degradation on D1/10V photocatalyst (a) MeCN solvent (b) MeCN solvent along with O_2 purging.

6.3.7 Plausible mechanism

Figure 6.13 displays a schematic diagram for the photocatalytic mechanism of CIP degradation. The VB and CB edge positions of Cd-doped Ag_2O and $BiVO_4$ were derived from results presented in subsections 6.3.2 and 6.3.3. Under visible light irradiation, both Cd doped Ag_2O (D1) and $BiVO_4$ (V0) parts of the composite got photo-excited. The photoexcited electrons of the D1 component quenched the photoexcited VB holes in $BiVO_4$. Such a Z-scheme electron transfer mechanism causes the accumulation of photoexcited holes in the D1's VB and electrons in the $BiVO_4$ CB. CIP molecules got oxidized on the holes in the VB of D1. DFT calculations indicate that H_2O molecules also oxidize on D1's VB, producing oxygen (O_2). As discussed earlier, MeCN control experiments also indirectly proved water oxidation. The photoexcited electrons in the $BiVO_4$ CB further reduce the O_2 molecules to form superoxide (O_2^{-}) radicals. The O_2^{-} also degrade CIP (H. Zhang et al., 2019). The scavenging experiment results support this photocatalytic mechanism involving the main reactive species, i.e., h^+ and O_2^{-}.

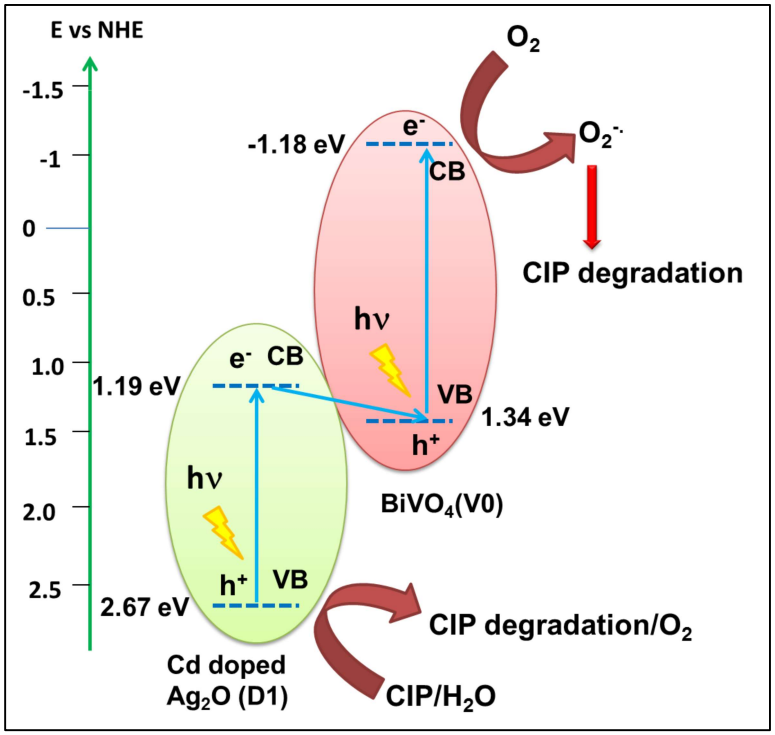

Figure 6.13 A schematic of the mechanism proposed based on the experimental and DFT calculation results.

6.4 Conclusions

Cd-doping of Ag_2O shifted the VB position drastically relative to Ag_2O. Such doping had little effect on the bandgap of the material. DFT formation energy calculations showed that Cd substituted Ag in the Ag_2O lattice. The XRD evidence also supported this result. The Cd-doped Ag_2O nanoparticles were effective photocatalysts for CIP degradation but with extremely poor recyclability. The second part of the investigation coupled $BiVO_4$ with Cd-doped Ag_2O nanostructures. These composites were efficient Z-scheme photocatalysts for CIP and also exhibited appropriate recyclability. DFT calculations demonstrated H_2O activation on Cd-doped Ag_2O. The DFT results indicate that the appreciably more positive VB of the Cd-doped Ag_2O can oxidize water molecules to produce oxygen. The latter is reduced by photoexcited

electrons accumulated on $BiVO_4$ to superoxide radicals. DFT calculations support this result. Parallelly, the results of scavenging (and the MeCN control experiments) indicate CIP oxidation on photoexcited VB holes in the (Cd-doped $Ag_2O/BiVO_4$) composite. Such a self-sustaining photocatalytic cycle increases the recyclability of composite significantly. Thus, doping of small bandgap semiconductors can change their electronic structure appreciably. Moreover, their composite with another visible range bandgap semiconductor can produce a new photocatalyst.